Catalysis Letters
https://doi.org/10.1007/s10562-020-03250-8

Effect of Calcination Temperature on Activity of Fe_2O_3–Al_2O_3 Nanocomposite Catalysts in CO Oxidation

Anna M. Kremneva[1] · Alexander V. Fedorov[1] · Olga A. Bulavchenko[1] · Yury V. Knyazev[2] · Andrey A. Saraev[1] · Vadim A. Yakovlev[1] · Vasily V. Kaichev[1]

Received: 10 March 2020 / Accepted: 1 May 2020

Abstract

Nanocomposite Fe–Al oxide catalysts were prepared by the melting of iron and aluminum nitrates with the subsequent calcination in air at different temperatures. It was found that the catalysts calcined at 450 °C are more active in the oxidation of CO than the catalysts calcined at 700 °C. X-ray diffraction and X-ray photoelectron spectroscopy showed that all the catalysts consist of hematite, α-Fe_2O_3 nanoparticles, and Al_2O_3 in an amorphous state. Iron oxide is the active component, which provides the oxidation of CO, while alumina is a texture promoter. The increase in the calcination temperature leads to a minor increase in the average size of hematite nanoparticles and an insignificant decrease in the specific surface area. Kinetic measurements showed that the oxidation of CO over the Fe–Al catalysts calcined at 450 and 700 °C proceeds with the activation energy of 61–69 and 91 kJ/mol, respectively. This means that the low-temperature and high-temperature catalysts contain different active species. Temperature-programmed reduction with CO indicated that the decrease in the calcination temperature improves the reducibility of the Fe-Al nanocomposites. According to ^{57}Fe Mössbauer spectroscopy, the low-temperature catalysts contain hydrated iron oxides (acagenite and ferrihydrite) and a significant amount of highly defective hematite, which is absent in the high-temperature catalyst. These species can provide the enhanced activity of the low-temperature catalysts in the oxidation of CO.

Graphic Abstract

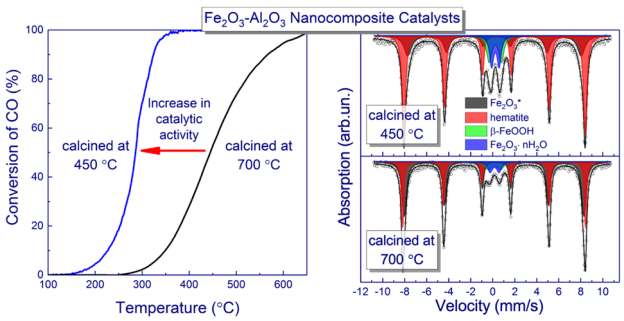

Keywords Environmental catalysis · Nanostructure · Gasification · Oxidation · Mössbauer spectroscopy

1 Introduction

Nowadays, issues of improving the environment attract increasing attention all over the world. The most discussed topic is the purification of automobile exhaust gases [1, 2], although the problem of utilization of various industrial wastes, including sludge formed during the treatment of

✉ Vasily V. Kaichev
vvk@catalysis.ru

[1] Boreskov Institute of Catalysis, 630090 Novosibirsk, Russia

[2] Kirensky Institute of Physics, Federal Research Center KSC SB RAS, 660036 Krasnoyarsk, Russia

Published online: 12 May 2020

sewage, is an equally important task [3]. The easiest way to utilize such waste is to burn it for energy production. However, since industrial wastes such as sawdust, rice husk, or sludge are a low-calorie fuel, the use of flame combustion is not effective, and it is necessary to use catalytic technologies [4]. It was shown that gasification and combustion of resulting gases in a fluidized catalyst bed is a promising technology for the waste utilization [5–7]. Since the CO oxidation is the rate determining step in this process [8], the catalysts used should exhibit high activity in this reaction. Recently, we have shown that Fe_2O_3–Al_2O_3 nanocomposite catalysts prepared by the melting of iron and aluminum nitrates with their subsequent calcination at 700 °C are acceptable for this technology [9]. The catalysts are low-cost, highly effective in the CO oxidation, and eco-friendly. According to the X-ray diffraction (XRD) study, the catalysts consist of mainly Fe_2O_3 and Al_2O_3 phases. Alumina is in an amorphous state, whereas iron oxide forms nanoparticles with the hematite structure. At that, the Al^{3+} cations are partially dissolved in the Fe_2O_3 lattice. The activity of the nanocomposite catalysts depends on Fe concentration, and its maximum is achieved when the Fe_2O_3 content is approximately 82 wt%. The oxidation of CO proceeds via the Mars–van Krevelen mechanism, in which Fe^{3+} is partially reduced to Fe^{2+} by CO and then is oxidized back by O_2 from the gas phase [8, 10, 11]. Alumina is a structural promoter, which stabilizes the intermediate magnetite phase [12]. Herein we present the results of our further study of the Fe–Al nanocomposite catalysts. We have found that a decrease in the calcination temperature to 450 °C leads to a significant increase in their catalytic activity in the CO oxidation. To elucidate this effect, we investigated the chemistry and structure of the catalysts by XRD, X-ray photoelectron spectroscopy (XPS), Mössbauer spectroscopy, temperature-programmed reduction with CO (TPR-CO), and N_2 adsorption technique.

2 Experimental

The catalysts were prepared by the melting of mixtures of nitrates $Fe(NO_3)_3{\cdot}9H_2O$ and $Al(NO_3)_3{\cdot}9H_2O$. First, the nitrates were mixed mechanically in the required molar ratios, and then the mixture was heated to give a homogeneous melt of crystal hydrate salts and was kept at a temperature of 200 °C until water was completely removed. Finally, the resulting dry powder was calcined at 450 °C for 1 h in air and then cooled in a flow of nitrogen to room temperature. The catalysts were referred to as the low-temperature Fe_xAl_{100-x} catalysts, where x corresponded to the Fe_2O_3 content (wt%). The reference catalyst containing 82 wt% of Fe_2O_3 was prepared by the same manner, but the calcination temperature was 700 °C. This catalyst was referred to as the high-temperature $Fe_{82}Al_{18}$-700 catalyst.

The catalytic tests were performed using a flow fixed bed reactor. The sample powder under study (fraction 0.25–0.50 mm) was first strongly diluted with an inert material (quartz sand) in the 1:5 ratio and then loosely packed into a tubular quartz reactor with an inner diameter of 2.4 mm and a length of 10 mm; the catalyst layer height was 1.35 mm. During the experiments, a reactant mixture containing 1.0% CO, 20% O_2, and N_2 as a balance was passed through the reactor with a constant flow rate. The flows of CO, oxygen, and nitrogen were regulated separately with SEC-Z500 (Horiba, Japan) mass-flow controllers. Total gas hourly space velocity was 1.2×10^5 h^{-1}. The catalyst was heated from 100 to 500 °C with a constant rate of 5 °C/min. A TEST-1 gas analyzer (Boner, Russia) equipped with an IR optical sensor was used for the detection of CO and CO_2 at the reactor outlet. The catalytic activity was determined as the temperature when the CO conversion reached 50%. This light-off temperature was referred to as T_{50}. In addition, the apparent activation energy (E_a) was calculated by the Arrhenius plot using the initial section of the light-off curves when the CO conversion was in the range 2–15%.

The specific surface area (SSA) of the catalysts was calculated by the Brunauer–Emmett–Teller method using nitrogen adsorption isotherms measured at liquid nitrogen temperature with an automatic ASAP 2400 sorptometer (Micromeritics, USA).

The catalysts were studied by XRD using a D8 Advance diffractometer (Bruker, Germany) equipped with a Lynxeye linear detector. The diffraction patterns were obtained in the 2θ range from 20° to 80° with a step of 0.05° using the monochromatic Cu $K\alpha$ radiation (λ = 1.5418 Å). The phases were identified using the powder diffraction database PDF-4+. The average size of hematite nanoparticles was estimated as a size of coherently scattering domains (CSD) using the Scherrer equation to the most intense 104 peak, assuming a spherical shape of the nanoparticles.

The XPS study was performed using an X-ray photoelectron spectrometer (SPECS Surface Nano Analysis GmbH, Germany) equipped with a PHOIBOS-150 hemispherical electron energy analyzer, an XR-50 M X-ray source with a twin Al/Ag anode, and a FOCUS-500 ellipsoidal crystal monochromator. The core-level spectra were obtained under ultrahigh vacuum conditions using the monochromatic Al $K\alpha$ radiation ($h\nu = 1486.74$ eV). The charge correction was performed by setting the Al2p peak at 74.5 eV, corresponding to aluminum in Al_2O_3 [13]. In this case, the main peak in the C1s spectra was observed at 284.7 ± 0.2 eV. Relative concentrations of elements were determined from the integral intensities of the core-level spectra using the cross sections according to Scofield [14]. For detailed analysis, the spectra were fitted into several peaks after the background subtraction by the Shirley method using the CasaXPS software [15]. The line shapes

of the peaks were approximated by the product of Lorentzian and Gaussian functions with the exception of the main Fe2$p_{3/2}$ and Fe2$p_{3/2}$ peaks that were approximated by an asymmetric, so-called "LF", line shape [15, 16].

Temperature-programmed reduction was carried out in a 10% CO/He flow (20 sccm) using a ChemBET Pulsar TPR/TPD analyzer (QuantaChrome Inst, USA). Before an experiment, a sample (about 40 mg) was dried in a He flow at 150 °C for 20 min. Then the sample was heated with a constant heating rate (20 °C/min) from the ambient temperature to 1000 °C. The CO consumption was measured by a thermal conductivity detector. To exclude the effect of evolving CO_2 on the detector reading, a NaOH trap was placed between the reactor and the detector.

^{57}Fe Mössbauer spectra were obtained using a MS-1104Em spectrometer equipped with a 512-channels detector. The measurements were performed at room temperature using a ^{57}Co/Rh gamma-ray source, which was moved at a constant acceleration against the absorber sample. The Isomer shifts and the velocity scale were calibrated with respect to α-Fe foil. The hyperfine parameters were determined by fitting the raw spectra by a sum of the Lorentzian functions using the non-linear least squares method.

3 Results and Discussion

A series of the nanocomposite Fe–Al oxide catalysts calcined at 450 °C was prepared and tested in the CO oxidation. The Fe_2O_3 content in the catalysts was varied between 50 and 100 wt%. In addition, the $Fe_{82}Al_{18}$-700 catalyst calcined at 700 °C was prepared and tested for comparison. The main results are summarized in Table 1. Figure 1a shows the temperature dependence of the CO conversion for the catalysts. One can see that all the catalysts calcined at 450 °C are more active than the $Fe_{82}Al_{18}$-700 catalyst. The light-off temperature varies between 296 and 316 °C for the low-temperature catalysts, whereas the light-off temperature for the high-temperature catalyst is 445 °C. In good agreement with our previous data [9], the light-off temperature for the low-temperature catalysts depends on the Fe_2O_3 content non-monotonously (Fig. 1b). The light-off temperature achieves minimum when the Fe_2O_3 content is near 90 wt%.

The oxidation of CO is a heterogeneous reaction, which proceeds over the catalyst surface. This means that the catalytic activity may depend on the specific surface area of the catalyst. From this point of view, the catalytic activity is best characterized not by the light-off temperature but by the reaction rate measured at a certain temperature. Figure 2a shows the reaction rate of the CO oxidation measured at

Table 1 Specific surface area (SSA), light-off temperature (T_{50}), activation energy (E_a), and specific reaction rate of CO oxidation at 220 °C (W_{220}) for the Fe–Al nanocomposite catalysts

Composition	SSA (m^2/g)	T_{50} (°C)	E_a (kJ/mol)	W_{220} (10^2 ml min^{-1} m^{-2})
$Fe_{100}Al_0$	29	296	69 ± 5	4.8
$Fe_{90}Al_{10}$	91	279	61 ± 5	4.4
$Fe_{82}A_{18}$	79	286	61 ± 5	2.6
$Fe_{70}Al_{30}$	125	302	67 ± 5	1.1
$Fe_{50}Al_{50}$	182	316	65 ± 5	0.8
$Fe_{82}Al_{18}$-700	60	445	91 ± 5	0.04

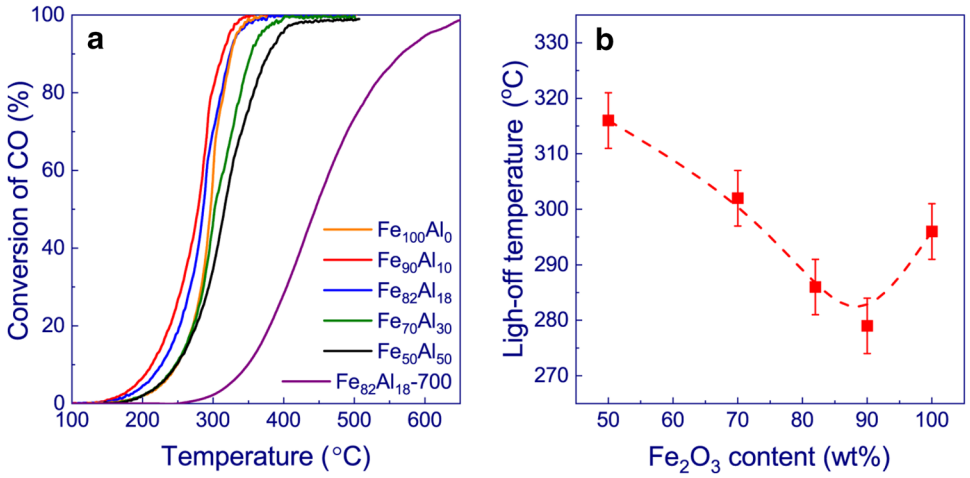

Fig. 1 **a** Conversion of CO as a function of reaction temperature for the catalysts under study. **b** Light-off temperature in CO oxidation of over the catalysts calcined at 450 °C versus Fe_2O_3 content

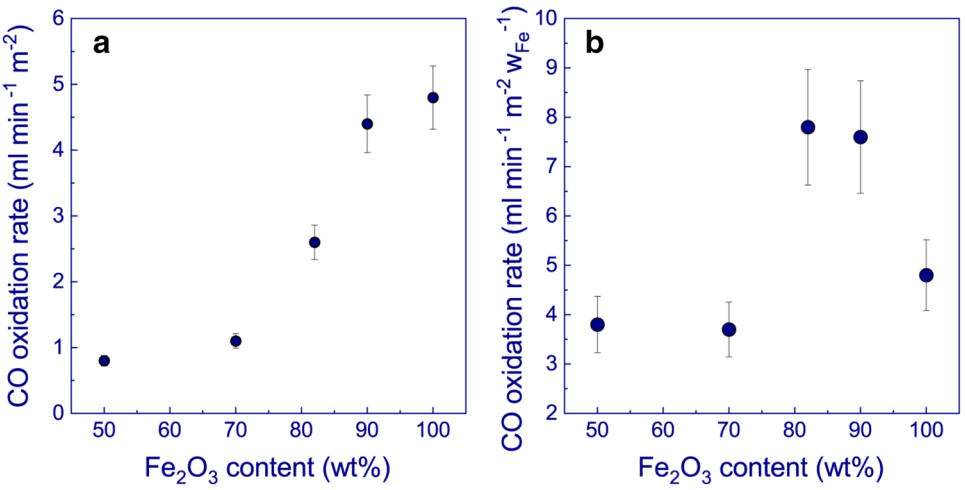

Fig. 2 **a** Dependence of the specific reaction rate of CO oxidation over the low-temperature Fe–Al catalysts measured at 220 °C versus the Fe_2O_3 content. **b** Dependence of the reaction rate normalized to SSA and W_{Fe} versus the Fe_2O_3 content

220 °C and normalized to the specific surface area of the catalyst versus the Fe_2O_3 content. One can see that this specific reaction rate (W_{220}) increases monotonously with the Fe_2O_3 content. Assuming that nanoparticles of alumina and iron oxide are homogeneously mixed, we can conclude that the rate of CO oxidation is determined mainly by the iron oxide content.

It should be noted that the activity of the catalyst depends on the content of iron oxide non-monotonously (Fig. 1b). The most active are the catalysts containing approximately 90 wt% iron oxide. This can be explained by the fact that on the catalyst surface there are not only particles of active iron oxide but also particles of aluminum oxide which do not take part in the oxidation of CO. Indeed, if we take into account the fraction of the surface occupied by iron oxide calculated on the basis of the XPS data (W_{Fe}), then the maximum oxidation rate of CO will be observed on catalysts containing 80–90 wt% Fe_2O_3 (Fig. 2b). The fraction W_{Fe} was calculated from the equation:

$$W_{Fe} = \frac{[Fe]/[Al]}{1 + [Fe]/[Al]},$$

where [Fe] and [Al] are relative atomic concentrations of Fe and Al, respectively, determined by XPS.

However, this effect cannot explain the enhanced activity of the low-temperature catalysts. The high-temperature $Fe_{82}Al_{18}$-700 catalyst provides W_{220} by two orders of magnitude lower than the low-temperature catalysts (Table 1). To elucidate the cause of this contradiction, we calculated the activation energy of the CO oxidation using the initial section of the light-off curves. We found that the oxidation of CO over the low-temperature Fe–Al catalysts is characterized by the activation energy of 61–69 kJ/mol. In contrast, the oxidation of CO over the $Fe_{82}Al_{18}$-700 catalyst proceeds with the activation energy of 91 kJ/mol (Table 1). Definitely, these differences indicate that the low-temperature and high-temperature catalysts contain different active species. Scattering in the activation energy of the low-temperature catalysts is due to experimental errors.

To elucidate the origin of the active species, the structure of the catalysts was investigated by XRD. The low-temperature catalysts exhibit well developed XRD patterns (Fig. 3), which match well only with α-Fe_2O_3. This oxide (hematite) has a rhombohedral structure with space group $R\bar{3}c$ (JCPDS No.330664). Al_2O_3 phases are not detected, indicating that

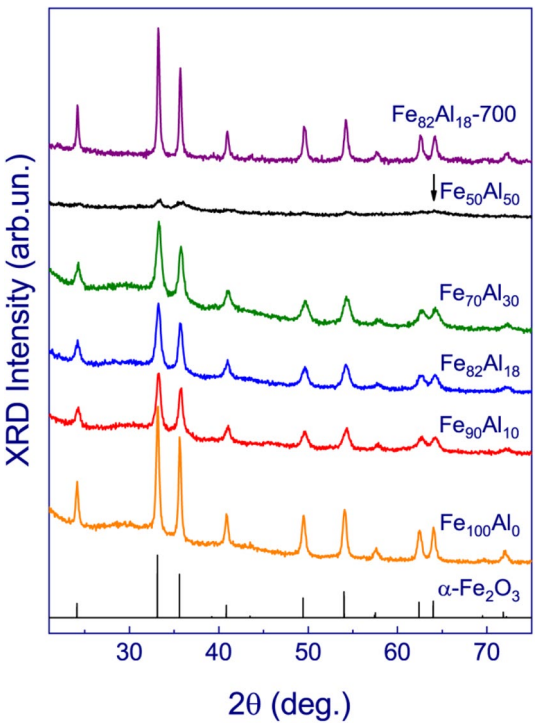

Fig. 3 X-ray diffraction patterns of Fe–Al nanocomposite catalysts. Arrow indicates the reflection of Al_2O_3

Table 2 Size of coherently scattering domains (CSD) of Fe_2O_3, lattice parameters (*a*, *b*, and *c*), and elementary cell volume of hematite (*V*) for the Fe–Al nanocomposites

Composition	CSD (Å)	$a=b$ (Å)	c (Å)	V (Å)
$Fe_{100}Al_0$	330	5.036	13.759	302.3
$Fe_{90}Al_{10}$	180	5.024	13.720	299.9
$Fe_{82}Al_{18}$	180	5.025	13.724	300.1
$Fe_{70}Al_{30}$	160	5.018	13.703	298.8
$Fe_{50}Al_{50}$	130	–	–	–
$Fe_{82}Al_{18}$-700	460	5.030	13.712	300.0

alumina is in an amorphous state. An exception is the XRD pattern of the $Fe_{50}Al_{50}$ catalyst, in which the features of hematite disappear, but a wide peak near 62–66° is observed. The latter indicates the presence of disperse Al_2O_3. In addition, the XRD patterns of the low-temperature catalysts contain a halo between 25° and 40°, which indicates the presence of amorphous Fe-containing phases. After calcination at 700 °C, this halo disappears and the hematite reflections become sharper. We estimated the average size of hematite nanoparticles as the size of coherently scattering domains using the Scherrer equation. The obtained results, as well as other crystal structure parameters, are listed in Table 2. For the low-temperature catalysts, a maximal average crystallite size of hematite (330 Å) is in the $Fe_{100}Al_0$ nanocomposite. However, the addition of even 10 wt% of alumina leads to an almost twofold decrease in the average size of hematite nanoparticles. Recently, we have shown that strong interaction of the alumina with iron oxide stabilizes the size of the iron oxide particles and prevents its sintering [12]. As a result, CSD of Fe_2O_3 decreases monotonously with an increase in the Al_2O_3 content. This process is accompanied by an increase in the specific surface area (Table 1). Due to sintering, the high-temperature catalyst is characterized by slightly lower SSA and larger CSD of hematite nanoparticles (460 Å).

It should be noted that the increase in the Al_2O_3 content leads also a decrease in the lattice parameters and the unit cell volume of Fe_2O_3 (Table 2). The volume of unit cell decreases from 302.3 to 298.8 $Å^3$ with the increase in the Al_2O_3 content. This means that Al^{3+} cations are incorporated into the hematite structure with the formation of a solid solution. Because the ionic radius of Al^{3+} is approximately 0.675 Å and the ionic radius of Fe^{3+} is approximately 0.785 Å [17], the formation of the solid solution should be accompanied by a decrease in the lattice parameters.

The TPR-CO study was performed using the $Fe_{82}Al_{18}$ catalysts calcined at 450 and 700 °C to examine their reducibility As seen from Fig. 4, the TPR curve of the high-temperature catalyst exhibits three regions of CO consumption: a sharp peak with a maximum at 426 °C with a

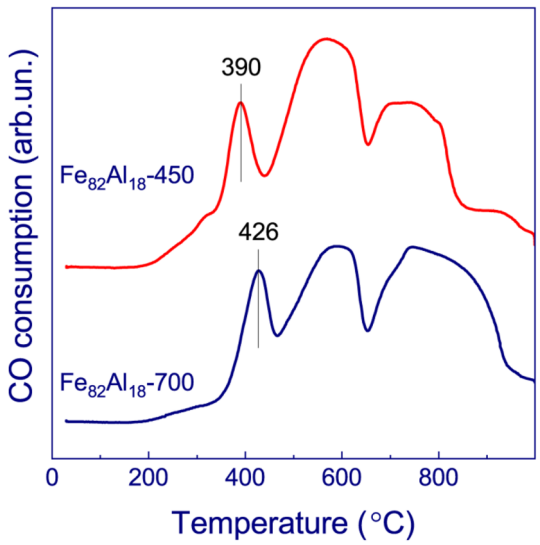

Fig. 4 TPR-CO profiles of Fe–Al nanocomposites calcined at 450 and 700 °C. The TPR profiles are normalized to the sample weight

weak shoulder at low temperatures and two wide peaks at 590 and 790 °C. According to our previous study by in situ XRD [9], these peaks correspond to indirect reduction of hematite with the formation of FeO intermediate phases ($Fe_2O_3 \rightarrow Fe_3O_4 \rightarrow FeO \rightarrow Fe$). The TPR curve of the low-temperature catalyst has a similar shape, but all the peaks are shifted to the lower temperatures. Moreover, the first sharp peak has a much more intense shoulder at low temperatures. We can speculate that this shoulder is due to reduction of the amorphous Fe-containing phases (Fig. 3). The amount of these amorphous phases is higher in the low-temperature catalyst than in the high-temperature catalyst, which can determine the enhanced activity of the nanocomposites calcined at 450 °C. Again, the first sharp peak in the TPR curve of the low-temperature catalyst, which corresponds to the reduction of hematite to magnetite, has a maximum at 390 °C, indicating that the low calcination temperature improves the reducibility of the Fe–Al nanocomposites. This effect is most likely associated with a smaller size of hematite nanoparticles and their high defectiveness (Table 2). In full agreement with the in situ XRD data [9], the total consumption of CO for the catalysts was 2.8–2.9 mol CO per mol Fe_2O_3. These values correspond to the almost stoichiometric reduction of Fe^{3+} to Fe^0.

The chemical state of iron in the low-temperature Fe–Al nanocomposite catalysts was examined by X-ray photoelectron spectroscopy. The corresponding Fe2*p* core-level spectra are presented in Fig. 5. The spectra contain two intense peaks near 711.2 and 724.9 eV and two weak peaks near 719.5 and 733.2 eV. The intense peaks are attributed to the Fe2$p_{3/2}$–Fe2$p_{1/2}$ spin-orbital doublet, while the weak peaks are due to shake-up satellites. According to the literature

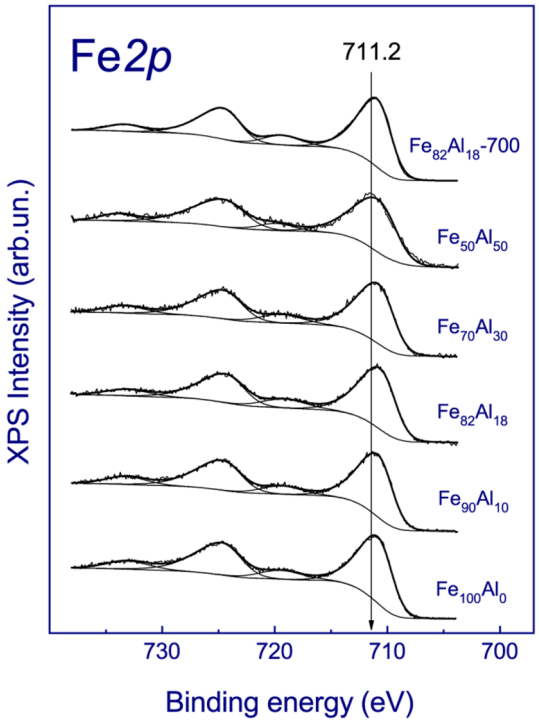

Fig. 5 Normalized Fe2*p* core-level spectra of the catalysts

[18–20], iron in the metallic state, FeO, and Fe_2O_3 is characterized by the Fe$2p_{3/2}$ binding energy in the ranges of 706.3–706.9, 709.1–710.7, and 710.6–711.5 eV, respectively. The shake-up satellites are not observed in the spectra of metallic iron and Fe_3O_4, while in the spectra of FeO and Fe_2O_3, they have the binding energy 5.7 and 8.1–8.3 eV higher than the Fe$2p_{3/2}$ peak. Taking into account the Fe$2p_{3/2}$ binding energy of 711.2 eV and the presence of the well-defined shake-up satellite at 719.5 eV, we can conclude that iron in the low-temperature catalysts is mainly in the Fe_2O_3 lattice. A similar Fe2*p* spectrum was observed for the high-temperature catalyst.

Thus, we have investigated the structure, chemistry, and specific surface area by XRD, XPS, and N_2 adsorption technique and have not observed any significant difference between the high-temperature and low-temperature Fe–Al nanocomposite catalysts. Unfortunately, XPS cannot identify a small concentration of Fe^{3+} cations in any other local environment other than the hematite structure. For example, the Fe2*p* spectra of α-Fe_2O_3 and γ-Fe_2O_3 are almost the same. In turn, XRD can identify only well-crystallized Fe-containing phases. This means that the catalysts may contain a small amount of Fe^{3+}-containing clusters, amorphous nanoparticles, as well as some other defective structures, that cannot be identified by XPS and XRD. To overcome this problem, we studied our catalysts by ^{57}Fe Mössbauer spectroscopy. This technique measures transitions between the sublevels of the nuclear ground state and the levels of the 14.4 keV

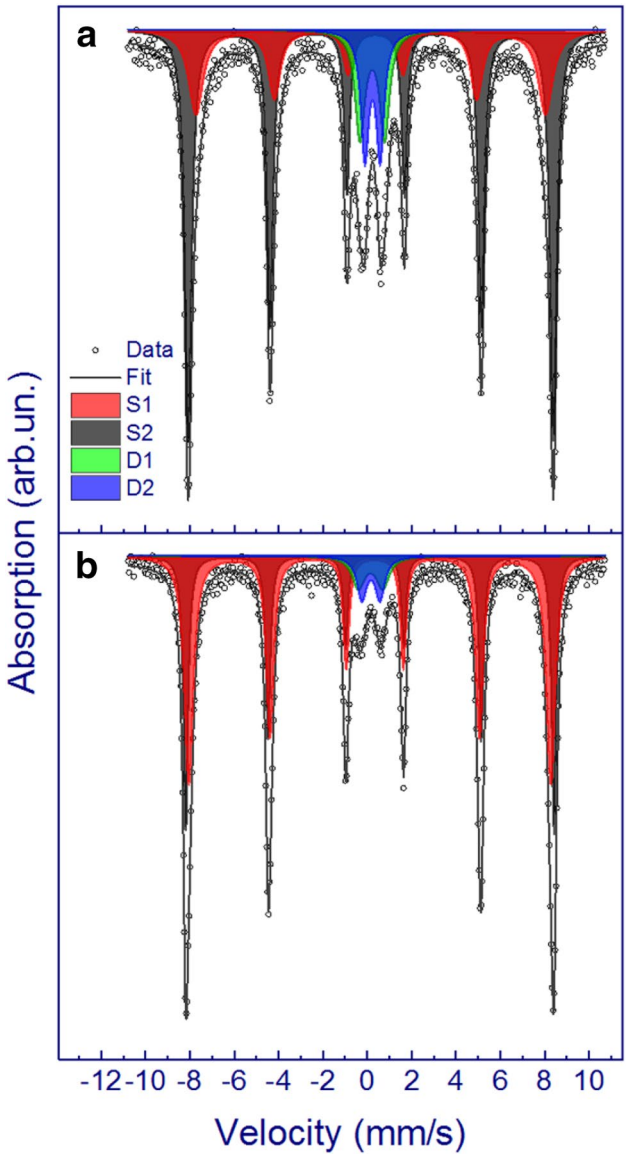

Fig. 6 Mössbauer spectra of $Fe_{82}Al_{18}$ nanocomposites calcined at 450 °C (**a**) and 700 °C (**b**)

nuclear excited states. Because hyperfine splitting depends on electronic quantities (such as charge distribution, symmetry, spin, and orbital angular momentum), the ^{57}Fe nucleus is a sensitive probe of the oxidation state of an iron site and its coordination environment [21].

The Mössbauer spectra of the $Fe_{82}Al_{18}$ nanocomposites calcined at 450 or 700 °C are presented in Fig. 6. Both spectra show a well-developed magnetic hyperfine splitting. It is obvious from the spectra shape that the sample composition is not single-phase. The spectrum of the low-temperature catalyst (Fig. 6a) can be fitted by at least two Zeeman sextets (S1 and S2) and two quadruple doublets (D1 and D2). The hyperfine parameters are listed in Table 3. It is well-known that hematite is antiferromagnetically ordered at room

Table 3 Hyperfine parameters estimated from the ^{57}Fe-Mössbauer spectra: the isomer shift (δ) relative to α-Fe at room temperature; the magnetic hyperfine field at ^{57}Fe nuclei (H_{hf}); the quadruple splitting (QS); the full width at half maximum of the Mössbauer line ($FWHM$); the heterogeneity of the magnetic environment of iron atoms in hematite structure (dH); the relative occupancy of the iron position (S)

	δ (±0.005 mm/s)	H_{hf} (±10 kOe)	QS (±0.02 mm/s)	$FWHM$, (±0.06 mm/s)	dH (±0.02 mm/s)	S (±3%)	Phase
$Fe_{82}Al_{18}$-450 °C							
S1	+0.370	491	−0.44	0.46	0.344	25	α-Fe_2O_3*
S2	+0.377	513	−0.44	0.30	0.078	55	α-Fe_2O_3-(1)
D1	+0.333	–	1.12	0.54	–	10	β-FeOOH
D2	+0.344	–	0.69	0.43	–	10	Fe_2O_3·nH_2O
$Fe_{82}Al_{18}$-700 °C							
S1	+0.376	508	−0.44	0.30	0.185	55	α-Fe_2O_3-(2)
S2	+0.375	517	−0.43	0.26	0	35	α-Fe_2O_3-(3)
D1	+0.297	–	1.10	0.70	–	5	β-FeOOH
D2	+0.315	–	0.81	0.53	–	5	Fe_2O_3·nH_2O

temperature and its Mössbauer spectra should exhibit one well-resolved sextet with a characteristic effective magnetic flux density and a considerable quadrupole splitting [21, 22]. Taking into account the hyperfine parameters of hematite ($\delta = 0.375$ mm/s and $H_{hf} = 517$ kOe [22]), we suppose that the S2 sextet, which is characterized by the isomer shift of 0.377 mm/s and the magnetic hyperfine field of 513 kOe, corresponds to well-crystallized hematite nanoparticles, α-Fe_2O_3-(1). The difference in the hyperfine parameters is due to shorter Fe–O and Fe–Fe distances because of the partial dissolution of Al^{3+} cations in the Fe_2O_3 lattice (Table 2). FWHM of the S2 sextet is 0.30 mm/s, which is consistent with a natural line-width of 0.24 mm/s. The other sextet could be also attributed to the hematite phase but only with a less ordered structure. Indeed, the S1 sextet is characterized by the magnetic hyperfine field of 491 kOe; a decrease in this parameter indicates an increase in the heterogeneity of magnetic and crystalline structures. Moreover, the S1 sextet is characterized by the large dH, that is, by the heterogeneity of the magnetic environment of iron atoms in the hematite structure. It can be assumed that the S1 sextet corresponds to highly defective hematite nanoparticles. This conclusion is confirmed by the large FWHM value of the S1 sextet (0.46 mm/s), which indicates a disordered or defective hematite structure. This phase is referred to as α-Fe_2O_3* (Table 2). Taking into account that the structure of hematite consists essentially of densely arranged Fe^{3+} cations in octahedral coordination with oxygen in hexagonal closest-packing, the defects can be associated with empty anion vacancies or with anion vacancies filled with OH-groups or H_2O. The D1 and D2 quadruple doublets can be attributed to hydrated iron oxides: β-FeOOH acagenite and Fe_2O_3·nH_2O ferrihydrite, respectively [21, 23–25]. Returning to the XRD data, a wide XRD peak between 25° and 40° could correspond to highly disperse β-FeOOH or Fe_2O_3·nH_2O [26]. After annealing, this XRD feature disappears.

The Mössbauer spectrum of the high-temperature nanocomposite has a similar shape and is also well described by two Zeeman sextets (S1 and S2) and two quadruple doublets (D1 and D2) (Fig. 6b). However, in this case, the sextets are characterized by other hyperfine parameters. Nevertheless, the S2 sextet undoubtedly corresponds to well-crystallized hematite nanoparticles ($\delta = 0.375$ mm/s, $H_{hf} = 517$ kOe, and $dH = 0$ mm/s). The increase in the calcination temperature leads to an increase in the magnetic hyperfine field, which indicates the annealing of the defects. The S1 sextet has similar hyperfine parameters ($\delta = 0.376$ mm/s and $H_{hf} = 508$ kOe) and is also attributed to hematite but with a small amount of defects [9]. We referred these species to as α-Fe_2O_3-(2) and α-Fe_2O_3-(3) hematite with different concentration of defects, respectively. Two other doublets correspond to hydrated iron oxides. It should be stressed that their intensity is half the intensity of D1 and D2 doublets in the spectrum of the low-temperature catalyst.

It should be noted that defects usually play a special role in catalytic reactions [27–30]. For example, it was shown that hydrogenation of CO proceed with a higher rate over a defective palladium surface than over atomically smooth Pd(111) surface [27]. The adsorption of methoxy species at defects on Fe_3O_4(001) promotes their disproportionation with the formation of methanol and formaldehyde [29]. Zhang et al. [30] showed the importance of oxygen defects on the surface of ZrO_2 for efficient activation of a C–H bond in C1–C4 alkanes in the catalytic dehydrogenation. Recently, it has been shown that the self-sustained oscillations in the oxidation of propane over Ni foil originate due to periodic oxidation and reduction of nickel and namely the formation of point defects in NiO which improve the reducibility of

nickel oxide provides the fast transition of the catalyst from the poorly active state to the highly active state [31].

Accordingly, we believe that some defects in the Fe–Al nanocomposites can affect their catalytic performance. Assuming the same Mössbauer probability for hematite and hydrated iron oxides, we evaluated the content of α-Fe_2O_3, α-$Fe_2O_3^*$, β-FeOOH, and $Fe_2O_3 \cdot nH_2O$ phases in the nanocomposites as the product from the resonance-line area S (Table 3). We found that the low-temperature nanocomposite consists of 55% of well-crystallized hematite nanoparticles, 25% of highly defective hematite nanoparticles, and 20% of hydrated iron oxides. In contrast, the high-temperature nanocomposite does not contain highly defective hematite, and moreover, the total amount of hydrated iron oxides is only 10%. This means that the catalysts calcined at 450 °C contain a large amount of highly defective hematite, which provides their enhanced catalytic activity in the CO oxidation. The hydrated iron oxides also can provide the enhanced catalytic activity. The calcination at 700 °C leads to annealing of the defects and, as a result, the $Fe_{82}Al_{18}$-700 catalyst exhibits lower activity in the CO oxidation. Taking into account the TPR-CO data we can conclude that the defects improve the reducibility of iron oxide that is important step in the oxidation of CO which proceeds via the redox Mars–van Krevelen mechanism [10].

4 Conclusion

The structure and chemistry of nanocomposite Fe–Al oxide catalysts prepared by the melting of iron and aluminum nitrates strongly depend on the calcination temperature. We found that the catalysts calcined at 450 and 700 °C exhibit different catalytic activities. The high-temperature catalyst, calcined at 700 °C, provides the specific rate of the CO oxidation two orders of magnitude lower than the low-temperature catalysts, calcined at 450 °C. According to kinetics measurements, the oxidation of CO over the low-temperature catalysts proceeds with the activation energy of 61–69 kJ/mol, whereas the oxidation of CO over the high-temperature catalyst proceeds with the activation energy of 91 kJ/mol. The XRD and TPR-CO results indicate that the decrease in the calcination temperature improves the reducibility of the Fe–Al nanocomposites due to the presence of hydrated iron oxides and highly defective hematite nanoparticles in the low-temperature catalysts. These defect phases provide the enhanced activity of the low-temperature catalysts in the oxidation of CO. The increase in the calcination temperature leads to annealing of the defects and partial decomposition of hydrated iron oxides.

Acknowledgements This work was supported by the Russian Science Foundation (Grant No. 17-73-20157). The experiments were performed using facilities of the shared research center "National center of investigation of catalysts" at Boreskov Institute of Catalysis. The authors thank A.Yu. Gladky for the TPR measurements and Z.S. Vinokurov for the XRD measurements.

Compliance with Ethical Standards

Conflict of interest The authors declare that they have no conflict of interest.

References

1. Keav S, Matam KS, Ferri D, Weidenkaff A (2014) Catalysts 4:226
2. Wang J, Chen H, Hu Z, Yao M, Li Y (2015) Catal Rev 57:79
3. Fytili D, Zabaniotou A (2008) Renew Sust Energy Rev 12:116
4. Prasad R, Kennedy LA, Ruckenstein E (1984) Catal Rev 26:1
5. Ismagilov ZR, Kerzhentsev MA (1999) Catal Today 47:339
6. Simonov AD, Yazykov NA, Vedyakin PI, Lavrov GA, Parmon VN (2000) Catal Today 60:139
7. Simonov AD, Fedorov NA, Dubinin YV, Yazykov NA, Yakovlev VA, Parmon VN (2013) Catal Ind 5:42
8. Fedorov AV, Saraev AA, Kremneva AM, Selivanova AV, Vorokhta M, Šmid B, Bulavchenko OA, Yakovlev VA, Kaichev VV (2020) Appl Catal A
9. Fedorov AV, Tsapina AM, Bulavchenko OA, Saraev AA, Odegova GV, Ermakov DY, Zubavichus YV, Yakovlev VA, Kaichev VV (2018) Catal Lett 148:3715
10. Saraev AA, Tsapina AM, Fedorov AV, Trigub AL, Bulavchenko OA, Vinokurov ZS, Zubavichus YV, Kaichev VV (2020) Radiat Phys Chem
11. Bulavchenko OA, Pochtar AA, Gerasimov EY, Fedorov AV, Chesalov YA, Saraev AA, Yakovlev VA, Kaichev VV (2020) Appl Catal A 590:117364
12. Bulavchenko OA, Vinokurov ZS, Saraev AA, Tsapina AM, Trigub AL, Gerasimov EY, Gladky AY, Fedorov AV, Yakovlev VA, Kaichev VV (2019) Inorg Chem 58:4842
13. Kosova N, Devyatkina E, Slobodyuk A, Kaichev V (2008) Solid State Ion 179:1745
14. Scofield JH (1976) J Electron Spectrosc Relat Phenom 8:129
15. Fairley N, CasaXPS: Processing Software for XPS A, SIMS and More (Casa Sofwware Ltd., 2018) www.casaxps.com
16. Matveev AV, Kaichev VV, Saraev AA, Gorodetskii VV, Knop-Gericke A, Bukhtiyarov VI, Nieuwenhuys BE (2015) Catal Today 244:29
17. Shannon RD (1976) Acta Cryst A 32:751
18. McIntyre NS, Zetaruk DG (1977) Anal Chem 49:1521
19. Descostes M, Mercier F, Thromat N, Beaucaire C, Gautier-Soyer M (2000) Appl Surf Sci 165:288
20. Yamashita T, Hayes P (2008) Appl Surf Sci 254:2441
21. Kuzmann E, Nagy S, Vértes A (2003) Pure Appl Chem 75:801
22. Lyubutin IS, Lin CR, Korzhetskiy YV, Dmitrieva TV, Chiang RK (2009) J Appl Phys 106:034311
23. Chambaere D, Govaert A, de Sitter J, de Grave E (1978) Solid State Commun 26:657
24. Murad E (1979) Clay Miner 14:273
25. Vieira AP, Berndt G, de Souza Junior IG, Di Mauro E, Paesano A, de Santana H, da Costa ACS, Zaia CTBV, Zaia DAM (2011) Amino Acids 40:205
26. Yatsenko DA, Pakharukova VP, Tsybulya SV, Matvienko AA, Sidel'nikov AA (2012) J Struct Chem 53:548
27. Rupprechter G, Kaichev VV, Unterhalt H, Morkel M, Bukhtiyarov VI (2004) Appl Surf Sci 235:26
28. Vattuone L, Savio L, Rocca M (2008) Surf Sci Rep 63:101

29. Gamba O, Hulva J, Pavelec J, Bliem R, Schmid M, Diebold U, Parkinson GS (2017) Top Catal 60:420
30. Zhang Y, Zhao Y, Otroshchenko T, Lund H, Pohl M-M, Rodemerck U, Linke D, Jiao H, Jiang G, Kondratenko EV (2018) Nat Commun 9:3794
31. Kaichev VV, Saraev AA, Gladky AY, Prosvirin IP, Knop-Gericke A, Bukhtiyarov VI (2019) Catal Lett 149:313